Radio science for connecting humans to information systems / L'homme connecté

A statistical assessment of ambient electromagnetic field using body-worn multiaxial sensors

Approche statistique de l'estimation du champ électromagnétique ambiant avec un capteur multi-axial porté par l'utilisateur

Christophe Roblin

LTCI, Télécom ParisTech & CNRS, Communications & Electronics Dept., 46, rue Barrault, 75013 Paris, France

A R T I C L E   I N F O

A B S T R A C T

The electromagnetic field exposure of the population due to wireless communications originates from both down-link and up-link emissions. Although the main contribution comes generally from the latter (e.g., higher by three to five orders of magnitude for the 2G), the former must be considered as well, because they are continual, and as contributions can be competitive for some cases (e.g., in femtocells). Sensor and exposimeter networks (NW) can be deployed by the operators themselves (to enrich feedback information from their own NW) or by independent external stakeholders such as regulatory agencies or local authorities. When sensors are directly worn by a user, body proximity effects – notably the *masking* effect – can introduce significant errors in the ambient field measurement. A methodology of the statistical assessment of this harmful effect is proposed in this article. It is mainly based on electromagnetic simulations (and partly on measurements) of a triaxial sensor – composed of three orthogonal wideband probes devoted to the evaluation of the field components – placed at different positions of a set of whole body phantoms. The main original contribution of the proposed approach is that both the isolated sensor calibration procedure and the assessment of the measurement errors are based on statistical analyses accounting for the propagation environment. The quantitative results are obtained using statistical channel models for polarimetric and non-polarimetric measurements in various propagation scenarios. Some quantitative results examples are presented. Eventually, preliminary corrections schemes are proposed.

© 2015 Académie des sciences. Published by Elsevier Masson SAS. All rights reserved.

R É S U M É

L'exposition de la population aux ondes électromagnétiques dues aux communications radio émane tant des émissions descendantes que montantes. Bien que la contribution dominante provienne généralement de ces dernières (supérieures de trois à cinq ordres de grandeur pour la 2G par exemple), les premières doivent également être prises en compte, notamment parce qu'elles sont permanentes, mais aussi parce que les deux contributions peuvent être compétitives dans certains cas (par exemple dans les *femtocells*). Des réseaux de capteurs et d'exposimètres peuvent être déployés par les opérateurs eux-mêmes (leur permettant d'enrichir les informations remontées par leur propre réseau) ou par des

E-mail address: christophe.roblin@telecom-paristech.fr.

acteurs extérieurs indépendants, tels que des organismes de contrôle réglementaire ou des collectivités locales. Si les capteurs sont directement portés par l'utilisateur, les effets de proximité du corps – notamment l'effet de masquage – peuvent introduire des erreurs très significatives dans la mesure du champ ambiant. Nous proposons dans cet article une méthodologie d'estimation statistique de cet effet néfaste. L'approche est majoritairement fondée sur des simulations électromagnétiques (et partiellement sur des mesures) d'un capteur triaxial – constitué de trois sondes large bande placées orthogonalement dédiées à la mesure des composantes du champ – placé à différentes positions de fantômes « corps entier ». L'originalité principale de cette contribution est qu'elle repose sur des analyses statistiques prenant en compte les conditions de propagation, que ce soit dans la procédure de calibration du capteur isolé ou dans l'évaluation des erreurs de mesure. Les résultats quantitatifs sont obtenus à partir de modèles statistiques de canaux, pour des mesures polarimétriques ou non, pour différents scénarios de propagation. Quelques résultats quantitatifs sont présentés. Pour terminer, des méthodes envisageables de correction encore à l'étude sont présentées.

1. Introduction

The Electromagnetic Field (EMF) exposure of the population due to wireless communications (2G, 3G, 4G and WLANs) originates both from Down-Link (DL) emissions incoming from Base Stations (BS) or Access Points (AP), and from Up-Link (UL) ones produced by the terminals (cell phones, tablets and laptops). Although the main contribution comes generally from the latter, the former must be considered as well because they are continual (whereas UL ones are intermittent and time limited), and as both contributions can be competitive for some cases (e.g., in femtocells). Note however that in this case, the EMF levels are particularly low. Hence, today a new paradigm regarding EMF exposure should be envisaged, considering more global approaches (in a manifold sense) because of the variety of radio emissions. To this end, new exposure indicators must be defined, merging both UL and DL emissions, considering the exposure of the population in given areas (instead of the "individual" one) and based on statistical approaches (instead of focussing only on worst cases that can be rare events). For example, one of the main objectives of the EU FP7 project *Lexnet* [1] is to propose innovative technical solutions to reduce the exposure level of the population, in a global way, without affecting the quality of service. The possible improvements are investigated in every parts of the system, both in terms of technology (antennas, sensitivity, wake-up strategy, Radio Resource Management, power control, etc.) and in terms of architectures and network (NW) management (heterogeneous networks, offloading, densification, etc.). To this end, a new *Exposure Index* (*EI*) aggregating all sources of exposure due to wireless NWs (merging both UL and DL emissions) and considering populations globally, their terminals usages, Radio Access Technologies (RATs from 2G to 4G), cells types (macro to femto), environments (urban, rural, indoor, ...), etc., is defined [2,3], and estimated statistically. The DL contribution is related to the field strength to which the user is exposed. This field level can be estimated via the NW to which the user is connected, or thanks to information collected by disseminated field sensors or personal dosimeters worn by some users (*exposimeters*). For the operators, the latter bring complementary or exogenous information (from other NWs and from or about other (non-) users). Beyond operators, sensor and exposimeter NWs can be deployed by independent external stakeholders such as regulatory agencies or local authorities.

This paper addresses the issue of the field level assessment and more specifically its evaluation with exposimeters. The main technical challenge resides in the modelling of the measurement errors of body-worn sensors, induced by proximity effects, notably the *masking effect* of the body, and, as far as possible their correction. The principal purpose of this article is to present a methodology of the statistical assessment of this harmful effect, which must be for example distinguished from the *shadowing* which is a pure channel effect. Note that the analysis of the other field measurement sources of uncertainty – e.g., traffic load, PHY layer structure, handover mechanism, etc., which are RAT specific, and measurement protocols (period of the day, duration, sampling rate, static or not, etc.) – are out of the perimeter of this work. The main specificity of the proposed approach is that both the isolated sensor calibration procedure and the assessment of the measurement errors are based on statistical analyses accounting for the propagation environment. The quantitative results are obtained using statistical channel models for polarimetric and non-polarimetric measurements in various propagation scenarios. A measurement campaign reported in [7] was first carried out with a triaxial sensor attached at three different locations on a whole body phantom (for a few distances to the body). Besides, electromagnetic simulations were performed with a simplified model of this sensor and a few anthropomorphic numerical phantoms (inhomogeneous, MRI based) [8]. Then, as the number of anthropomorphic phantoms are limited, more EM simulations with simplified homogeneous models (based on canonical geometries) have been initiated, as modifying their anthropometric characteristics is much easier.

The article is organised as follows: issues and adopted methodology are presented in Section 2, some characteristics and calibration procedures of the isolated sensor are described in Section 3, some elements about the numerical phantoms are discussed in Section 4, examples of statistical results and possible correction schemes are presented in Sections 5 and 6, developments and future works, and conclusions, are drawn in Sections 7 and 8.
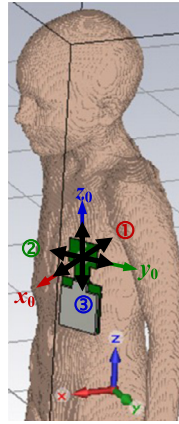
Fig. 1. (Color online.) Sensor model worn by a child girl phantom showing the global and local coordinate systems.

2. Issue and methodology

2.1. Used formalism

The antenna transfer function (ATF) $\mathcal{H}(f, \theta, \varphi)$ [10,11] is computed (in the transmitting or receiving mode) from the Far Field (FF) calculated over 0.7–6 GHz with the Time Domain solver of CST Microwave Studio®, for each axial probe and possible configuration. The definition used for the ATFs is recalled hereafter for clarity:

$$\mathbf{E}_p^\infty(f, \hat{\mathbf{r}}) = \frac{\mathrm{e}^{-jkr}}{r} \sqrt{\frac{\eta_0}{4\pi}} \mathcal{H}_p^\mathrm{T}(f, \hat{\mathbf{r}}) a_p \tag{1}$$

$$b_p(f, \hat{\mathbf{r}}) = \mathrm{e}^{-j\mathbf{k}_i \cdot \mathbf{r}} \sqrt{\frac{4\pi}{\eta_0}} \mathcal{H}_p^\mathrm{R}(f, \hat{\mathbf{r}}) \cdot \mathbf{E}_i(\mathbf{k}_i, \mathbf{r}) = -\frac{1}{2} j \sqrt{\frac{4\pi}{\eta_0}} \frac{c}{\omega} \mathcal{H}_p^\mathrm{T}(f, \hat{\mathbf{r}}) \cdot \mathbf{E}_{i0} = \chi(f) \mathcal{H}_p^\mathrm{T}(f, \hat{\mathbf{r}}) \cdot \mathbf{E}_{i0} \tag{2}$$

where a_p (resp. b_p) is the incident (the received) wave at the pth probe port, $\mathcal{H}^\mathrm{R}$ (resp. $\mathcal{H}^\mathrm{T}$) is the ATF in the receiving (resp. transmitting) mode, $\hat{\mathbf{r}}$ is the unit radial vector (to be read as "$\hat{\mathbf{r}} \equiv (\theta, \varphi)$" as a function argument), η_0 the free space impedance, ω the angular frequency, k the wavenumber, $\mathbf{E}_p^\infty$ the FF radiated by the pth probe, $\mathbf{E}_i(f, \mathbf{r})$ the electric field of the incident plane wave, $\mathbf{k}_i$ its wave vector, and $\mathbf{E}_{i0} = \mathbf{E}_i(f, \mathbf{0})$ denotes the impinging field at the origin, chosen at the centre of the sensor spherical ground (common to the three orthogonal dipoles used as probes). All relevant quantities (realized gain G_r, radiation or total efficiencies and (loaded) antenna factor *AF*, etc.) can be computed from the ATF, for each polarization. In particular, for this ATF definition, the realized gain is more precisely given by a very simple relationship:

$$G_r(f, \hat{\mathbf{r}}) = \left\| \mathcal{H}^\mathrm{T} \right\|^2 = \mathcal{H}^\mathrm{T} \cdot \mathcal{H}^{\mathrm{T}*} = \left| \mathcal{H}_\theta^\mathrm{T} \right|^2 + \left| \mathcal{H}_\varphi^\mathrm{T} \right|^2 = G_\mathrm{r}^\theta + G_\mathrm{r}^\varphi$$

In the following, $\mathcal{H}^\mathrm{T}$ will be used (instead of $\mathcal{H}^\mathrm{R}$) and the coefficient χ will be omitted because all considered signals will be normalized in a way or another (either calibrated or normalized to a signal of reference) so that this coefficient (depending only on the frequency) will systematically disappear in the considered quantities.

2.2. Objectives and methodology

The EMF assessment, measured with exposimeters, is prone to additional errors and uncertainty due to the presence of the body (in addition to those due to the imperfections of the probes). Mainly two physical effects must be considered [4–6]. First the *masking effect*, which mostly occurs when most of the energy comes from a direction apposite to the user side on which the sensor is placed on; the EM flow is screened by an "effective capture area" of the body, whereas only a fraction reaches the sensor thanks to diffraction (the higher the frequency, the weaker the proportion). This effect is consequently strongly directional. Second, a more general loss effect related to the energy absorbed by the body (i.e. dissipated by human tissues) and to the antenna/body coupling. The statistical estimation of the field measurement error consequently depends on: (i) The propagation conditions in a Multi Path (MP) environment, notably its angular spectrum (in LOS/NLOS situations) and its depolarization effects, (ii) The frequency band and the RAT, (iii) The subject stature, corpulence and posture, and, (iv) the sensor positioning on the user.

The methodology adopted here to analyse these effects is the following:

(1) compute (or measure) the ATF $\mathcal{H}_p^\mathrm{T}(f, \theta, \varphi)$ [10] of each orthogonal probe $p \in \{x, y, z\}$ (or $\{1, 2, 3\}$) in the transmitting mode, for both the isolated and the worn sensor;

(2) perform the corresponding simulations/measurements for a statistically representative set of configurations, including anthropometric characteristics and sensor positions;
(3) as described in detail in [6], thanks to the reciprocity theorem, the signal received by each probe can then be computed from the transfer functions and the MPCs (Multi Path Components) by linear combination $b_p(f) \propto \sum_{n=1}^{N} \boldsymbol{\mathcal{H}}_p^{\mathrm{T}}(f, \theta_n, \varphi_n) \cdot \mathbf{E}_{i,n}(\theta_n, \varphi_n)$, considering channel models for a set of propagation scenarios (a simplified version of the WINNER2/+ models has been chosen here);
(4) normalise the received signals of the worn sensor by the corresponding signals received by the isolated sensor (considered as reference signals), *averaged* over each frequency band and representative statistical samples for a given set of propagation scenarios, thanks to Monte Carlo simulations.

The set of anthropometric and positioning parameters associated with the channel characteristics constitutes the input stochastic space. All EM simulations are performed in the Time Domain (FIT) with CST MWS®, mainly with a computation server (4 dual core multiprocessor with 128 GB RAM, accelerated with 4 Tesla® 2050/2070 GPUs). Depending on the size of the EM problem (related to the size of the phantom and desired accuracy), the number of mesh cells varies between 50 and 150 Mcells and the CPU computation time ranges typically between 1 and 8 h.

A set of simulations with non-homogeneous anthropomorphic phantoms (voxel models from the Virtual Family® (VF) suit [12]) are performed as a first step. The number of these models and the diversity of their morphological characteristics are limited. Besides, simulations with these realistic models are computationally demanding, and the tools of morphological deformation (posture, overweight, etc.) are rare, difficult to use, time-consuming and imperfect. Hence, simulations are then performed with simplified homogeneous models designed from canonical geometries (spheroids, cylinders, truncated cones, etc.). The advantages are twofold: these models are parameterizable and computationally more efficient. The physical properties of these models (i.e. the dispersive law of the permittivity of the effective medium) can be approximately estimated thanks to the simulations performed with the non-homogeneous anthropomorphic models.

3. Isolated sensor

The triaxial field sensor is composed of three orthogonal wideband probes (electric dipole-like antennas with a common ground) operating over 0.5–6 GHz. The numerical model used (Fig. 1) is a simplified version of a sensor developed by the company SATIMO® (integrated for example in their EME Spy 140® dosimeter). The modelling of the received signal on each probe in a multipath environment was already described in §2 [6]. This section is hence devoted to the calibration procedure and to the evaluation of the measurement errors of the field.

Usually, the simplest way to assess the measurement accuracy of multi-probes field sensors is to consider the deviation from omnidirectionality or "isotropy" of the probes. The procedure can be based on the computation of the partial (co-polar) realized gains $G_{\mathrm{r}}^{\mathrm{co}}(f, \hat{\mathbf{r}})$, of the "vertical" probe on the one hand, and on the combined "horizontal" probes on the other hand, averaged over each RAT frequency band (Fig. 2), i.e.:

$$\bar{G}_{\mathrm{v}}^{\theta}(f_{\mathrm{RAT}}, \theta, \varphi) = \frac{1}{\Delta f_{\mathrm{RAT}}} \int_{\Delta f_{\mathrm{RAT}}} G_{r,\mathrm{v}}^{\theta}(f, \theta, \varphi)\mathrm{d}f = \frac{1}{\Delta f_{\mathrm{RAT}}} \int_{\Delta f_{\mathrm{RAT}}} \left|\mathcal{H}_3^{\theta}(f, \theta, \varphi)\right|^2 \mathrm{d}f$$

$$\bar{G}_{\mathrm{h}}^{\varphi}(f_{\mathrm{RAT}}, \theta, \varphi) = \frac{1}{\Delta f_{\mathrm{RAT}}} \int_{\Delta f_{\mathrm{RAT}}} G_{r,\mathrm{h}}^{\varphi}(f, \theta, \varphi)\mathrm{d}f = \frac{1}{\Delta f_{\mathrm{RAT}}} \int_{\Delta f_{\mathrm{RAT}}} \sum_{p=1}^{2} \left|\mathcal{H}_p^{\varphi}(f, \theta, \varphi)\right|^2 \mathrm{d}f \tag{3}$$

then, from the computation of their angular "variance" (or standard deviation), expressed in dB, i.e.:

$$\sigma_{G_{\mathrm{v}}^{\theta}}^{90}(f_{\mathrm{RAT}}) = \left\{\mathrm{Var}_{\varphi}\left[\left.\bar{G}_{\mathrm{v}}^{\theta}\left(f_{\mathrm{RAT}}, \frac{\pi}{2}, \varphi\right)\right|_{\mathrm{dB}}\right]\right\}^{1/2}, \quad \varphi \in [0, 2\pi]$$

$$\sigma_{G_{\mathrm{h}}^{\varphi}}^{90}(f_{\mathrm{RAT}}) = \left\{\mathrm{Var}_{\varphi}\left[\left.\bar{G}_{\mathrm{h}}^{\varphi}\left(f_{\mathrm{RAT}}, \frac{\pi}{2}, \varphi\right)\right|_{\mathrm{dB}}\right]\right\}^{1/2}, \quad \varphi \in [0, 2\pi]$$

$$\sigma_{G_{\mathrm{v}}^{\theta}}^{\Delta\theta}(f_{\mathrm{RAT}}) = \left\{\mathrm{Var}_{\theta,\varphi}\left[\left.\bar{G}_{\mathrm{v}}^{\theta}(f_{\mathrm{RAT}}, \theta, \varphi)\right|_{\mathrm{dB}}\right]\right\}^{1/2}, \quad \varphi \in [0, 2\pi], \theta \in \left[\frac{\pi}{2} - \Delta\theta, \frac{\pi}{2} + \Delta\theta\right]$$

$$\sigma_{G_{\mathrm{h}}^{\varphi}}^{\Delta\theta}(f_{\mathrm{RAT}}) = \left\{\mathrm{Var}_{\theta,\varphi}\left[\left.\bar{G}_{\mathrm{h}}^{\varphi}(f_{\mathrm{RAT}}, \theta, \varphi)\right|_{\mathrm{dB}}\right]\right\}^{1/2}, \quad \varphi \in [0, 2\pi], \theta \in \left[\frac{\pi}{2} - \Delta\theta, \frac{\pi}{2} + \Delta\theta\right] \tag{4}$$

However, this procedure does not take into account several phenomena, such as the cross-polarization component of the probes, and the angular and depolarization properties of the propagation channel in a MP environment. This results most often in an underestimation of the error, as will be shown hereafter (see Tables 1 and 2).

Over the lower frequency range (typically below ~ 1.5–2 GHz), probes are small-size antennas behaving approximately as Hertzian dipoles (or *doublets*), for which it is easy to prove that the signal received by each probe p is proportional to
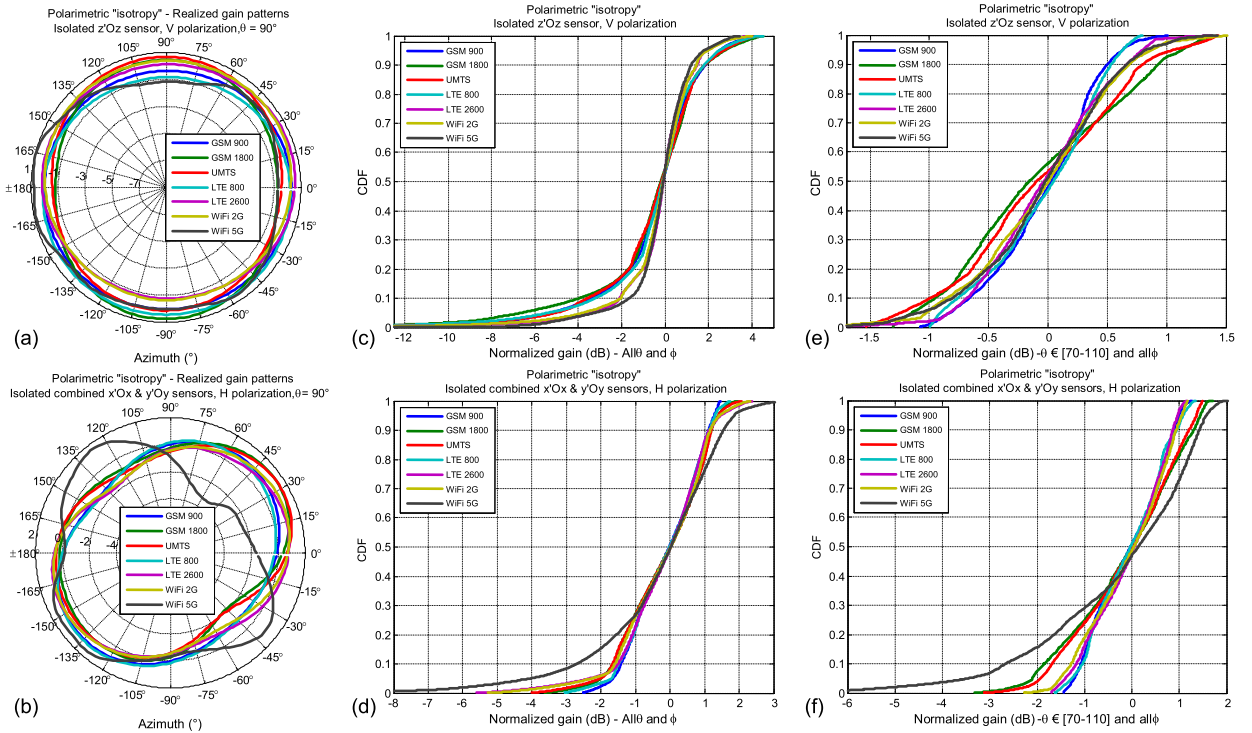
Fig. 2. (Color online.) Realized gain patterns (averaged over each band) $\bar{G}_v^\theta, \bar{G}_h^\varphi$ (a–b) and their variability over the whole sphere (c–d) or a part of it (e–f).

the field component parallel to its axis, i.e.: $b_p(f) = \kappa_p(f) \cdot E_{i0,p}$ where κ_p is a complex coefficient independent of $\hat{\mathbf{r}}$, $E_{i0,p}$ with $p \in \{x, y, z\}$ (or $\{1, 2, 3\}$) is the pth component of the field $\mathbf{E}_{i0}$ and where:

$$\mathbf{E}_{i0} = \sum_{n=1}^{N} \left(E_n^\theta \hat{\boldsymbol{\theta}}_n + E_n^\varphi \hat{\boldsymbol{\varphi}}_n \right) \tag{5}$$

is the total incoming field resulting from N MPCs of DoA (θ_n, φ_n), evaluated at the centre of the sensor. The following calibration procedure is based on the assumption that this simple relationship roughly holds over the whole band. However, its specificity is that it is based on a statistical approach taking into account the characteristics of the channel. This approach is more realistic (and actually more accurate) than "classical" calibration methods (e.g., based on measurements in anechoic chamber, only resorting to the intrinsic characteristics of the sensor) because closer to real usages [6,7]. For each statistical realization of the channel, the received signal, averaged in the frequency domain over each RAT band, is hence *approximated* as:

$$\bar{b}_p \left(f_{\text{RAT}}, n_{\text{sp}}, Env \right) \cong \left[\frac{1}{\Delta f_{\text{RAT}}} \int_{\Delta f_{\text{RAT}}} \left| \kappa_p(f, Env) \right|^2 \left| E_{i0}^{(p)}(n_{\text{sp}}, Env) \right|^2 \mathrm{d}f \right]^{1/2} \tag{6}$$

where $E_{i0}^{(p)}(n_{\text{sp}}, Env) = \sum_{n=1}^{N_{n_{\text{sp}}}} E_{i0,n}^{(p)}(\hat{\mathbf{r}}_n, Env)$, $p \in \{x, y, z\}$ (or $\{1, 2, 3\}$), considering a channel model (here WINNER2/+) for each type of environment Env (UMa – Urban Macrocell –, UMi – Urban Microcell –, Indoor, for LOS or NLOS conditions, O2I – Outdoor to Indoor –, etc.; see Appendix A (Table 5)). The parameter n_{sp} denotes a statistical realization of the channel model comprising $N_{n_{\text{sp}}}$ MPCs, $E_{i0,n}^{(p)}$ being the pth component of the electric field of the nth MPC (incoming from the DoA $\hat{\mathbf{r}}_n$). A Monte Carlo (MC) analysis allows us to define a reference signal as the expectation of the received signal for a given environment:

$$\bar{b}_p^{\text{ref}} (f_{\text{RAT}}, Env) = \left\langle \bar{b}_p \left(f_{\text{RAT}}, n_{\text{sp}}, Env \right) \right\rangle_{\text{stat}} \cong \overline{\kappa}_p (f_{\text{RAT}}, Env) \cdot \left\langle \left| E_{i0}^{(p)}(n_{\text{sp}}, Env) \right| \right\rangle_{\text{stat}} \tag{7}$$

from which the calibration coefficients can be approximately deduced:

$$\overline{\kappa}_p (f_{\text{RAT}}, Env) \cong \frac{\bar{b}_p^{\text{ref}} (f_{\text{RAT}}, Env)}{\langle |E_{i0}^{(p)}(n_{\text{sp}}, Env)| \rangle_{\text{stat}}} \tag{8}$$
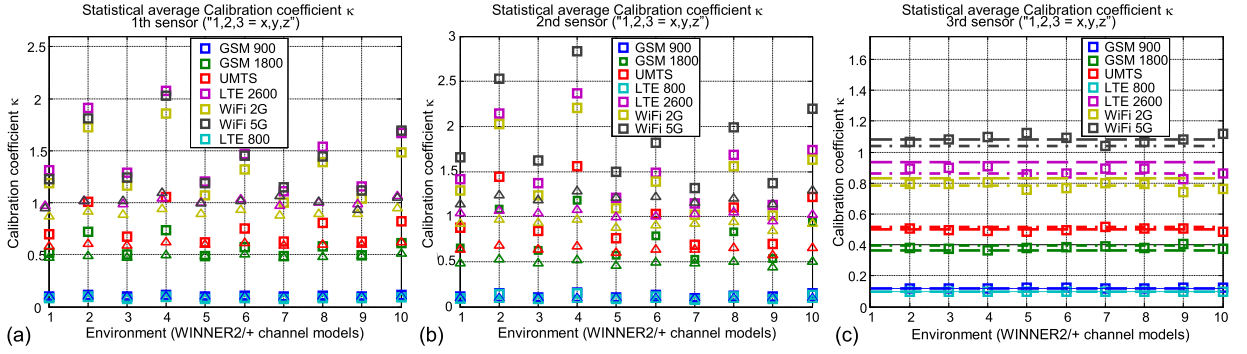
Fig. 3. (Color online.) Statistical calibration coefficients $\overline{\kappa}_p$ for each probe ("axis") of the simulated isolated sensor and ten WINNER2/+ environments (□); removing the CxPC of each horizontal probe (△); and intrinsic calibration coefficients for the vertical probe ($3^{\text{rd}}/z'Oz)\overline{\kappa}_v^{90}$ (–) and $\overline{\kappa}_v^{70-110}$ (—·).

The results for ten environments are given in Fig. 3. Note that the odd (resp. even) environment numbers *Env* correspond to NLOS (resp. LOS) environments (see Appendix A). The total number of samples in the MC analyses is set to $N_s = 10\,000$.

Considering that the propagation environment is generally not known by the measurement system (or the user), average coefficients can be computed a priori and used by the system. As can be seen in Fig. 3, $\overline{\kappa}_p$ weakly depends on the environment for the NLOS cases so that NLOS coefficients $\overline{\kappa}_p^{\text{NLOS}}(f_{\text{RAT}}) = \langle\overline{\kappa}_p(f_{\text{RAT}}, Env)\rangle_{\text{NLOS}}$ can be defined. Except for the two lowest frequency bands, this "average approach" is significantly less accurate for the LOS cases. This question will be briefly discussed in Section 7. Intrinsic calibration coefficients are also considered. Among various possibilities, two definitions based on the angular averaging of the realized gains are proposed in (9) and (10). Their values, independent of the environment by construction, are shown in Fig. 3 for comparison, only for the 3rd probe (vertically oriented, see Fig. 1), as there computation is slightly different for the horizontal ones.

$$\overline{\kappa}_v^{90}(f_{\text{RAT}}) = \overline{\kappa}_3^{90}(f_{\text{RAT}}) = \frac{1}{2\pi}\int_0^{2\pi}\left[\overline{G}_v^\theta\left(f_{\text{RAT}}, \frac{\pi}{2}, \varphi\right)\right]^{1/2}\mathrm{d}\varphi$$

$$\overline{\kappa}_h^{90}(f_{\text{RAT}}) = \overline{\kappa}_{(1,2)}^{90}(f_{\text{RAT}}) = \frac{1}{2\pi}\int_0^{2\pi}\left[\overline{G}_h^\varphi\left(f_{\text{RAT}}, \frac{\pi}{2}, \varphi\right)\right]^{1/2}\mathrm{d}\varphi \tag{9}$$

$$\overline{\kappa}_v^{\Delta\theta}(f_{\text{RAT}}) = \frac{1}{4\pi\sin\Delta\theta}\int_{\pi/2-\Delta\theta}^{\pi/2+\Delta\theta}\int_0^{2\pi}\left[\overline{G}_v^\theta(f_{\text{RAT}}, \theta, \varphi)\right]^{1/2}\sin\theta\mathrm{d}\theta\mathrm{d}\varphi$$

$$\overline{\kappa}_h^{\Delta\theta}(f_{\text{RAT}}) = \frac{1}{4\pi\sin\Delta\theta}\int_{\pi/2-\Delta\theta}^{\pi/2+\Delta\theta}\int_0^{2\pi}\left[\overline{G}_h^\varphi(f_{\text{RAT}}, \theta, \varphi)\right]^{1/2}\sin\theta\mathrm{d}\theta\mathrm{d}\varphi \tag{10}$$

The estimated field for each realization is computed as:

$$\hat{E}_{i0}^{(p)}(f_{\text{RAT}}, n_{\text{sp}}, Env) = \overline{b}_p(f_{\text{RAT}}, n_{\text{sp}}, Env)/\overline{\kappa}_p(f_{\text{RAT}}, Env), \quad p \in \{x, y, z\} \tag{11}$$

from the signal received at each probe computed as:

$$b_p(f, n_{\text{sp}}, Env) = \sum_{n=1}^{N_{n_{\text{sp}}}}\left[\mathcal{H}_p^\theta(f, \hat{\mathbf{r}}_n)E_{i0,n}^\theta(\hat{\mathbf{r}}_n) + \mathcal{H}_p^\varphi(f, \hat{\mathbf{r}}_n)E_{i0,n}^\varphi(\hat{\mathbf{r}}_n)\right], \quad p = 1, 2, 3 \tag{12}$$

and averaged over each RAT frequency band, as:

$$\overline{b}_p(f_{\text{RAT}}, n_{\text{sp}}, Env) = \left[\frac{1}{\Delta f_{\text{RAT}}}\int_{\Delta f_{\text{RAT}}}\left|b_p(f, n_{\text{sp}}, Env)\right|^2\mathrm{d}f\right]^{1/2} \tag{13}$$

Examples of the statistics (Cumulative Distribution Function – CDF) of the relative error of the field assessment are given hereafter for various environments. The relative error is computed from the exact values of the field components in the *Cartesian* coordinate system (because all MPCs projected in this system add linearly), i.e.: $E_{i0}^{(p)}(n_{\text{sp}}) =$

$\sum_{n=1}^{N_{n_{sp}}} E_{i0,n}^{(p)}$, $p \in \{x, y, z\}$. In practice, these field components are computed from the "vertical" (θ-component) and "horizontal" (φ-component) generated from the channel model in *spherical* coordinates, as:

$$E_{i0}^x(n_{sp}) = \left| \sum_{n=1}^{N_{n_{sp}}} \left[E_{i0,n}^\theta \cos\theta_n \cos\varphi_n - E_{i0,n}^\varphi \sin\varphi_n \right] \right|, \qquad E_{i0}^y(n_{sp}) = \left| \sum_{n=1}^{N_{n_{sp}}} \left[E_{i0,n}^\theta \cos\theta_n \sin\varphi_n + E_{i0,n}^\varphi \cos\varphi_n \right] \right|$$

$$E_{i0}^z(n_{sp}) = \left| \sum_{n=1}^{N_{n_{sp}}} E_{i0,n}^\theta \sin\theta_n \right| = E_{i0}^v(n_{sp}), \qquad E_{i0}^h(n_{sp}) = \left[E_{i0}^{x^2} + E_{i0}^{y^2} \right]^{1/2} \quad \text{and} \quad E_{i0}(n_{sp}) = \left[E_{i0}^{h^2} + E_{i0}^{z^2} \right]^{1/2} \tag{14}$$

The relative errors for polarimetric and non-polarimetric measurements are expressed in dB as:

$$\hat{e}_{i0}^{z,h}(n_{samp}) = 20 \log \frac{\hat{E}_{i0}^{z,h}(n_{samp})}{E_{i0}^{z,h}(n_{samp})} \quad \text{and} \quad \hat{e}_{i0}(n_{samp}) = 20 \log \frac{\hat{E}_{i0}(n_{samp})}{E_{i0}(n_{samp})} \tag{15}$$

from which their statistics can be computed. The CDFs for LOS indoor (model No. 2) and NLOS/LOS UMa (models Nos. 9 and 10) environments are presented in Fig. 4 and the first moments are given in Tables 1 and 2.

Note that the relative error is low for the NLOS case (notably for the "vertical" probe and the non-polarimetric measurement combining all probes signals) because the channel angular spread (in particular in azimuth) tends to compensate for the non-perfect omnidirectionality/isotropy of the sensor. The bias (Table 1) is low by construction, particularly for the vertical component ($|\mu_{\hat{e}_{i0}^z}| < 0.05$ dB) and the total field strength ($|\mu_{\hat{e}_{i0}}| < 0.15$ dB). The relative error of the horizontal component is larger because:

- first, the radiation pattern of the combined horizontal probes is less omnidirectional;
- second, its values are lower (the channel cross polarization ratio XPR_E is large because its depolarization effect is moderate, and the BS/AP are supposed to transmit in vertical polarization), and consequently more sensitive to the "numerical noise" (such as the radiation patterns sampling and interpolation or the numerical errors of the EM simulations);
- third, because of the imperfect polarization purity of the horizontal probes (associated with the high XPR_E).

Note as well that, e.g., the error standard deviation is larger in indoor LOS conditions than in UMa LOS ones (by about 0.4 to 0.8 dB), because the XPR_E of the former is higher ($\mu/\sigma = 11/4$ dB compared to $8/4$ dB) with comparable Rice K factors ($\mu/\sigma = 7/6$ dB against $7/3$ dB). The error on the vertical component and on the total field amplitude is also low for LOS cases because the vertical component is even more dominant in this case and the omnidirectionality of the vertical probe is good.

This can be checked by artificially removing the cross-polarization component (CxPC) of the two horizontal probes, as follows. The transfer function of each probe can be written as:

$$\boldsymbol{\mathcal{H}}_p = \mathcal{H}_p^\theta \hat{\boldsymbol{\theta}} + \mathcal{H}_p^\varphi \hat{\boldsymbol{\varphi}} = \mathcal{H}_p^{co} \hat{\boldsymbol{\theta}}_p + \mathcal{H}_p^{cx} \hat{\boldsymbol{\varphi}}_p = \mathcal{H}_p^x \hat{\mathbf{x}} + \mathcal{H}_p^y \hat{\mathbf{y}} + \mathcal{H}_p^z \hat{\mathbf{z}} \tag{16}$$

where $(\hat{\boldsymbol{\theta}}, \hat{\boldsymbol{\varphi}})$ are the transverse unit vectors of the general spherical coordinate system (Fig. 1) in which all the probes are measured (or simulated). The co ($\mathcal{H}_p^{co}$) and cross-polarization ($\mathcal{H}_p^{cx}$) components of each dipole-like probe are expressed in their own "natural" (or "local") coordinate system for which the probe is aligned along the $z_p' O z_p$ axis. For example, for the 1st probe, oriented along $x'Ox$, we have: $\hat{\mathbf{x}}_1 = -\hat{\mathbf{z}}$, $\hat{\mathbf{y}}_1 = \hat{\mathbf{y}}$ and $\hat{\mathbf{z}}_1 = \hat{\mathbf{x}}$ (rotation of $\pi/2$ around $y'Oy$). The components of the transfer functions in each system are consequently related by rotations, i.e.: $(\mathcal{H}_p^{co}, \mathcal{H}_p^{cx})^t = \mathfrak{R}_p (\mathcal{H}_p^\theta, \mathcal{H}_p^\varphi)^t$ which must be expressed in spherical coordinates. The matrices $\mathfrak{R}_p$ are orthogonal, so that $\mathfrak{R}_p^{-1} = \mathfrak{R}_p^t$, where the superscript "t" represents the transposition. For the two horizontal probes, we have:

$$\begin{pmatrix} \hat{\boldsymbol{\theta}}_p \\ \hat{\boldsymbol{\varphi}}_p \end{pmatrix} = \mathfrak{R}_p \begin{pmatrix} \hat{\boldsymbol{\theta}} \\ \hat{\boldsymbol{\varphi}} \end{pmatrix} \text{ with } \mathfrak{R}_1 = \frac{1}{D_1} \begin{pmatrix} -\cos\theta\cos\varphi & \sin\varphi \\ -\sin\varphi & -\cos\theta\cos\varphi \end{pmatrix} \text{ and } \mathfrak{R}_2 = \frac{1}{D_2} \begin{pmatrix} -\cos\theta\sin\varphi & -\cos\varphi \\ \cos\varphi & -\cos\theta\sin\varphi \end{pmatrix} \tag{17}$$

with: $D_1 = (1 - \sin^2\theta\cos^2\varphi)^{1/2}$ and $D_2 = (1 - \sin^2\theta\sin^2\varphi)^{1/2}$. Inversely: $(\mathcal{H}_p^\theta, \mathcal{H}_p^\varphi)^t = \mathfrak{R}_p^t (\mathcal{H}_p^{co}, \mathcal{H}_p^{cx})^t$.

For each MPC n, the output signal at each probe p is given by: $b_p^{(n)} = \boldsymbol{\mathcal{H}}_p(\hat{\mathbf{r}}_n) \cdot \mathbf{E}_{i0,n}(\hat{\mathbf{r}}_n)$. After cumbersome but elementary calculations, this reads:

$$b_1^{(n)} = -\frac{\mathcal{H}_1^{co}(\hat{\mathbf{r}}_n)}{D_1^{(n)}} E_{i0,n}^x(\hat{\mathbf{r}}_n) + \frac{\mathcal{H}_1^{cx}(\hat{\mathbf{r}}_n)}{D_1^{(n)}} \left[-\cos\theta_n E_{i0,n}^y(\hat{\mathbf{r}}_n) + \sin\theta_n \sin\varphi_n E_{i0,n}^z(\hat{\mathbf{r}}_n) \right]$$

$$b_2^{(n)} = -\frac{\mathcal{H}_2^{co}(\hat{\mathbf{r}}_n)}{D_2^{(n)}} E_{i0,n}^y(\hat{\mathbf{r}}_n) + \frac{\mathcal{H}_2^{cx}(\hat{\mathbf{r}}_n)}{D_2^{(n)}} \left[\cos\theta_n E_{i0,n}^x(\hat{\mathbf{r}}_n) - \sin\theta_n \cos\varphi_n E_{i0,n}^z(\hat{\mathbf{r}}_n) \right] \tag{18}$$
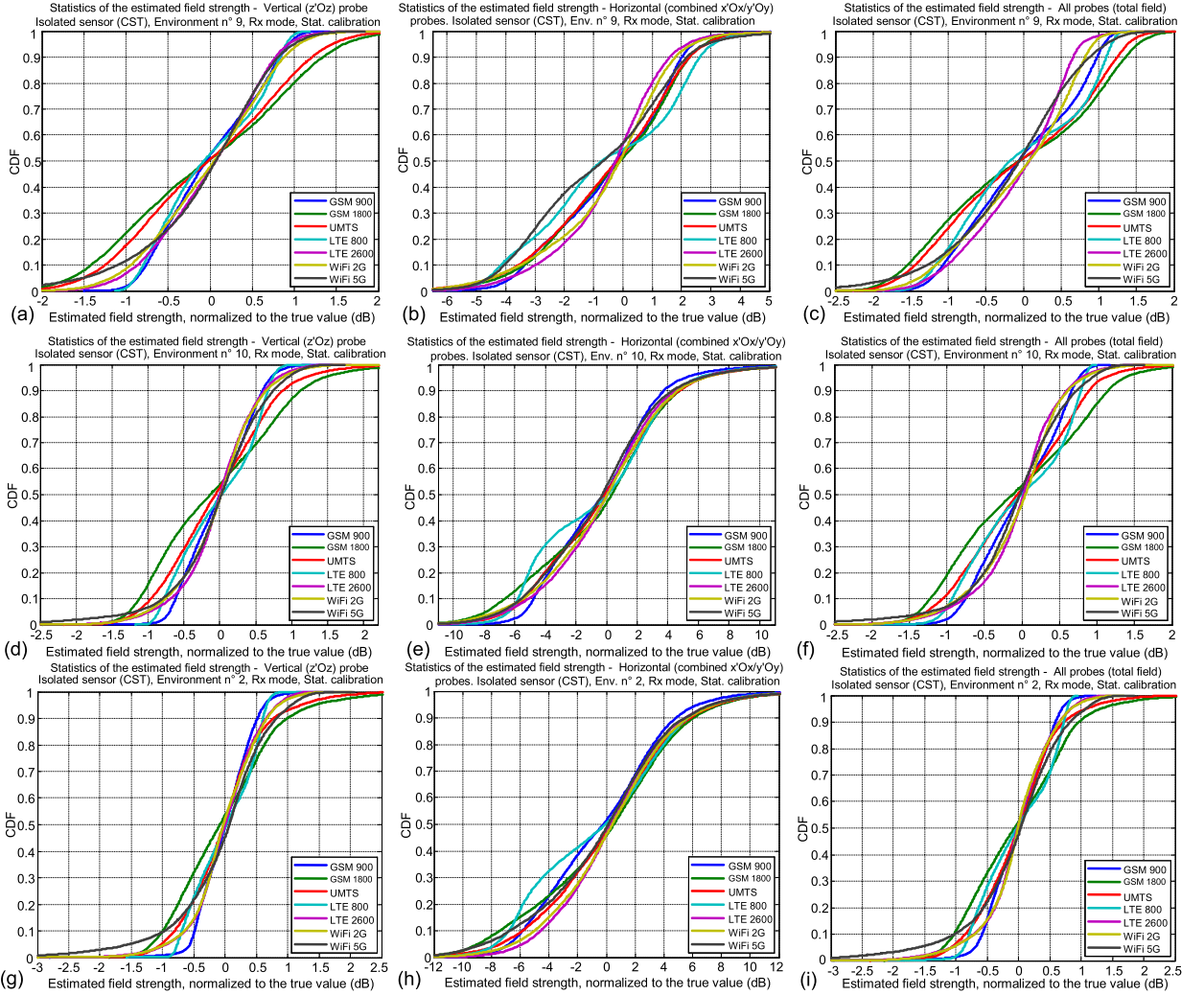
Fig. 4. (Color online.) Statistics ($N_s = 10\,000$) of the relative error of the field measurement (dB) with the isolated sensor for three WINNER2/+ environments: UMa NLOS, No. 9 (a–c); LOS, No. 10 (d–f) and LOS Indoor, No. 2 (g–i).

It is eventually easy from these computations to artificially "remove" the cross-polarization component of each horizontal probe, obtaining hence their "ideal responses" (Fig. 5). This operation is here restricted to the two horizontal probes, because first we made the assumption that the BS (or AP) transmit in vertical polarization, and second the depolarization effect of the channel is moderate for most of the scenarios (i.e. its XPR_E is high, roughly between 5 and 20 dB, but typically above 10 dB), so that the vertical probe is weakly affected. To more clearly picture these calculations, we can consider a sensor composed of perfect orthogonal doublets. Their ATF would read [11]:

$$\mathcal{H}_1(f, \hat{\mathbf{r}}) = -K(f)\sin\theta_1\hat{\boldsymbol{\theta}}_1 = K(f)\left(\cos\theta\cos\varphi\,\hat{\boldsymbol{\theta}} - \sin\varphi\,\hat{\boldsymbol{\varphi}}\right) = K(f)\left(\hat{\mathbf{x}} - \cos\theta_1\hat{\mathbf{r}}\right)$$

$$\mathcal{H}_2(f, \hat{\mathbf{r}}) = -K(f)\sin\theta_2\hat{\boldsymbol{\theta}}_2 = K(f)\left(\cos\theta\sin\varphi\,\hat{\boldsymbol{\theta}} + \cos\varphi\,\hat{\boldsymbol{\varphi}}\right) = K(f)\left(\hat{\mathbf{y}} - \cos\theta_2\hat{\mathbf{r}}\right)$$

$$\mathcal{H}_3(f, \hat{\mathbf{r}}) = -K(f)\sin\theta_3\hat{\boldsymbol{\theta}}_3 = -K(f)\sin\theta\,\hat{\boldsymbol{\theta}} = K(f)\left(\hat{\mathbf{z}} - \cos\theta\,\hat{\mathbf{r}}\right) \qquad (19)$$

giving $b_p^{(n)} = -[\mathcal{H}_p^{\text{co}}(\hat{\mathbf{r}}_n)/D_p^{(n)}]E_{i0,n}^{(p)}(\hat{\mathbf{r}}_n) = K(f)E_{i0,n}^{(p)}(\hat{\mathbf{r}}_n)$, $p = 1, 2, 3$ or $p \in \{x, y, z\}$, then $\bar{\kappa}_p(f_{\text{RAT}}) = \bar{K}(f_{\text{RAT}})$ because $b_p(f) = \sum_n b_p^{(n)} = K(f)\sum_n E_{i0,n}^{(p)}(\hat{\mathbf{r}}_n) = K(f)E_{i0}^{(p)}$, leading to a perfect evaluation of the field components.

Note that this "ideal" calibration procedure is not accessible *as is* in practice, as the CxPC is artificially removed in the numerical computations giving the above CDFs (following the calculations presented in (18)). It can be observed that the statistical dispersions are now almost the same for the two LOS environments (Fig. 5).
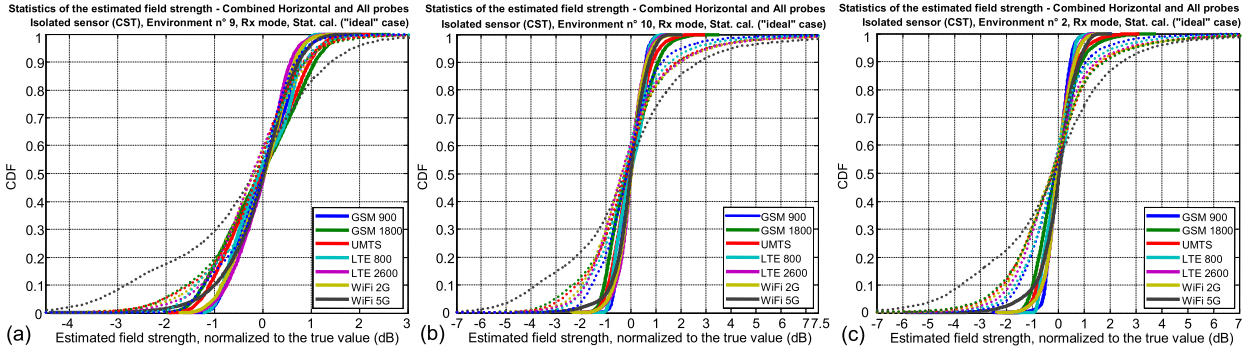
Fig. 5. (Color online.) Statistics ($N_s = 10\,000$) of the relative error of the field measurement (dB) with "ideal" probes for three WINNER2/+ environments: UMa NLOS, No. 9 (a), UMa LOS, No. 10 (b) and Indoor LOS, No. 2 (c). Total field strength (plain) and horizontal component (dot).
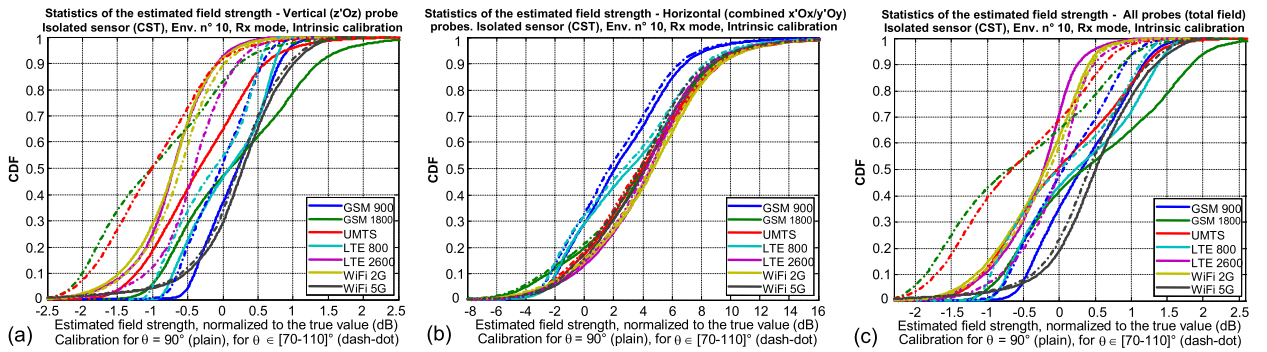

Fig. 6. (Color online.) Statistics of the relative error of the field measurement (dB) with the "intrinsic" calibration coefficients $\overline{\kappa}_{v,h}^{90}$ (plain) and $\overline{\kappa}_{v,h}^{70-110}$ (dash–dot) for the UMa LOS environment (No. 10).

Correction schemes of the CxPC of the horizontal probes are possible, but not straightforward, because, of course, the DoAs of the MPCs are not known (this would be of course much simpler in a single path environment). Anyway, an ongoing work on this topic will be proposed in a separate paper, as this aspect is beyond the scope of this article, which is primarily focused on the effects of the body proximity of the user on the field measurement.

Statistics of the error obtained with the "intrinsic" calibration coefficients are provided as an example for the UMa LOS environment. Despite the computation simplicity of these coefficients, their drawback is the introduction of a bias in the field estimation (particularly for the horizontal component) as can be observed in Fig. 6 and in Table 1. However, the variance is of course almost not affected (Table 2).

The measurement error assessment for these different calibration approaches are summarized in Table 1 and Table 2. In Table 1, errors which are theoretically unbiased by construction and very low in practice are generally not given, e.g.: $|\mu_{\hat{e}_i^z}|$, $|\mu_{\hat{e}_{i0}^{id}}| < 0.07$ dB (and $|\mu_{\hat{e}_{i0}^{id}}| < |\mu_{\hat{e}_{i0}}|$). The solid angle chosen for the "intrinsic" calibration corresponds to an elevation span of $\Delta\theta = \pm 20°$ (i.e. $\theta \in [70°, 110°]$).

In Table 2, only $\sigma_{\hat{e}_{i0}^z}$ is presented as $\sigma_{\hat{e}_{i0}^{z,90}} = \sigma_{\hat{e}_{i0}^{z,\Delta\theta}} = \sigma_{\hat{e}_{i0}^z}$; it is almost the same for the horizontal probes as $\sigma_{\hat{e}_{i0}^{h,90}} = \sigma_{\hat{e}_{i0}^{h,\Delta\theta}} \cong \sigma_{\hat{e}_{i0}^h}$ (in particular for NLOS cases) and for the total field ($\sigma_{\hat{e}_{i0}^{\Delta\theta}} \cong \sigma_{\hat{e}_{i0}^{90}}$). As can be observed in Table 2, resorting to purely intrinsic indicators such as the deviation to omnidirectionality with, e.g., $\sigma_{G_v^\theta}^{90}$ or $\sigma_{G_h^\theta}^{90}$ (irrespective of channel characteristics) underestimates the measurement error assessment (compared to $\tilde{e}_{i0}^z$ or $\tilde{e}_{i0}^h$), mainly because the probes cross-polar component is not taken into account. Conversely, integrating over the whole sphere ($\sigma_{G_v^\theta}^{all}$) over-estimates the error for the vertical component. Using intrinsic calibration coefficients ($\overline{\kappa}_{v,h}^{90}$, etc., as defines in (9) and (10)) introduces a bias, i.e. a mean error, compared to the "statistical" calibration (Table 1). However, this error is reasonably low in NLOS environments because their azimuthal angular spread is large. Inversely, in LOS conditions, the bias ($\mu_{\hat{e}_{i0}^{h,90}}$ or $\mu_{\hat{e}_{i0}^{h,\Delta\theta}}$) is really significant for the horizontal component (cf. Section 7 for additional comments). For the non-polarimetric measurements, the bias remains low even for the "worst" calibration procedures because the BSs (or APs) are supposed to transmit in vertical polarization and the channel depolarization effect is generally moderate.

Table 1
Isolated sensor – typical UMa (Env. Nos. 9 & 10) – field measurement error assessment: mean ("bias").

μ (dB)	UMa NLOS (Environment No. 9)												UMa LOS (Environment No. 10)											
	$\hat{e}_{i0}^{z,\overline{Env}}$	$\hat{e}_{i0}^{z,90}$	$\hat{e}_{i0}^{z,\Delta\theta}$	$\hat{e}_{i0}^{h}$	$\hat{e}_{i0}^{h,\overline{Env}}$	$\hat{e}_{i0}^{h,90}$	$\hat{e}_{i0}^{h,\Delta\theta}$	$\hat{e}_{i0}^{h,id}$	$\hat{e}_{i0}$	$\hat{e}_{i0}^{\overline{Env}}$	$\hat{e}_{i0}^{90}$	$\hat{e}_{i0}^{\Delta\theta}$	$\hat{e}_{i0}^{z,\overline{Env}}$	$\hat{e}_{i0}^{z,90}$	$\hat{e}_{i0}^{z,\Delta\theta}$	$\hat{e}_{i0}^{h}$	$\hat{e}_{i0}^{h,\overline{Env}}$	$\hat{e}_{i0}^{h,90}$	$\hat{e}_{i0}^{h,\Delta\theta}$	$\hat{e}_{i0}^{h,id}$	$\hat{e}_{i0}$	$\hat{e}_{i0}^{\overline{Env}}$	$\hat{e}_{i0}^{90}$	$\hat{e}_{i0}^{\Delta\theta}$
GSM 900	0.19	0.32	0.08	−0.36	**−1.15**	0.52	0.13	−0.12	−0.03	0.02	0.37	0.10	0.07	0.21	−0.03	−0.32	0.64	**2.44**	**2.04**	−0.08	−0.03	0.09	0.34	0.09
GSM 1800	0.46	0.84	−0.28	−0.33	**−2.45**	0.20	−0.11	−0.23	−0.06	0.11	0.75	−0.24	−0.17	0.20	−0.92	−0.28	0.90	**3.90**	**3.59**	−0.16	−0.06	−0.12	0.46	−0.56
UMTS	0.11	0.07	−0.61	−0.41	**−2.92**	0.08	−0.14	−0.22	−0.06	−0.26	0.09	−0.51	−0.26	−0.30	−0.98	−0.17	0.89	**4.14**	**3.92**	−0.14	−0.05	−0.22	0.04	−0.58
LTE 800	0.04	0.06	−0.16	−0.50	**−1.63**	0.71	0.29	−0.14	−0.04	−0.16	0.22	−0.04	0.03	0.06	−0.16	−0.48	0.72	**3.33**	**2.91**	−0.11	−0.03	0.07	0.29	0.06
LTE 2600	−0.52	−1.10	−0.81	−0.43	**−2.90**	0.60	0.32	−0.21	−0.06	−0.83	−0.78	−0.61	−0.15	−0.72	−0.43	−0.04	0.94	**4.42**	**4.14**	−0.10	−0.04	−0.11	−0.31	−0.09
Wi-Fi 2G	−0.42	−0.95	−0.85	−0.45	**−3.05**	0.57	0.35	−0.22	−0.06	−0.75	−0.66	−0.62	−0.22	−0.74	−0.64	−0.10	0.91	**4.53**	**4.32**	−0.12	−0.04	−0.17	−0.29	−0.23
Wi-Fi_33 5G	−0.06	−0.08	−0.14	−0.79	**−3.21**	−0.05	−0.40	−0.35	−0.15	−0.43	−0.06	−0.17	0.25	0.23	0.17	−0.40	0.90	**4.12**	**3.78**	−0.24	−0.07	0.26	0.48	0.39

Table 2
Isolated sensor – typical UMa (Env. No. 9 & 10) – field measurement error assessment: standard deviation.

σ (dB)	Omnidir./"Isotropy"						UMa NLOS (Environment No. 9)							UMa LOS (Environment No. 10)							
	$\sigma_{G_v^\theta}^{90}$	$\sigma_{G_h^\varphi}^{90}$	$\sigma_{G_v^\theta}^{\Delta\theta}$	$\sigma_{G_h^\varphi}^{\Delta\theta}$	$\sigma_{G_v^\theta}^{all}$	$\sigma_{G_h^\varphi}^{all}$	$\hat{e}_{i0}^{z}$	$\hat{e}_{i0}^{z,90}$	$\hat{e}_{i0}^{h}$	$\hat{e}_{i0}^{h,id}$	$\hat{e}_{i0}$	$\hat{e}_{i0}^{90}$	$\hat{e}_{i0}^{id}$	$\hat{e}_{i0}^{z}$	$\hat{e}_{i0}^{z,90}$	$\hat{e}_{i0}^{h}$	$\hat{e}_{i0}^{h,90}$	$\hat{e}_{i0}^{h,id}$	$\hat{e}_{i0}$	$\hat{e}_{i0}^{90}$	$\hat{e}_{i0}^{id}$
GSM 900	0.21	0.73	0.44	0.75	**2.4**	0.97	0.60	0.59	2.10	0.72	0.77	0.80	0.57	0.46	0.46	**3.58**	**3.67**	1.41	0.55	0.62	0.47
GSM 1800	0.49	0.95	0.70	1.14	**2.9**	1.14	1.05	1.05	2.32	0.99	1.11	1.10	0.88	0.90	0.90	**4.56**	**4.60**	1.98	0.93	1.03	0.86
UMTS	0.40	0.98	0.69	1.06	**2.6**	1.18	0.95	0.94	2.37	0.96	1.03	1.03	0.78	0.74	0.74	**4.22**	**4.37**	1.96	0.77	0.88	0.70
LTE 800	0.47	0.74	0.47	0.75	**2.6**	1.02	0.62	0.62	2.63	0.85	0.87	0.94	0.61	0.55	0.55	**4.37**	**4.38**	1.66	0.67	0.81	0.56
LTE 2600	0.45	0.80	0.52	0.76	**1.9**	1.24	0.64	0.63	1.88	0.92	0.65	0.68	0.51	0.53	0.53	**4.0**	**4.02**	1.93	0.55	0.53	0.50
Wi-Fi_33 2G	0.43	0.84	0.59	0.83	**2.1**	1.25	0.70	0.70	2.15	0.97	0.76	0.80	0.57	0.56	0.56	**4.24**	**4.31**	1.99	0.59	0.62	0.53
Wi-Fi_33 5G	0.59	1.48	0.57	1.7	**1.6**	1.91	0.78	0.78	2.55	1.60	0.86	0.88	0.71	0.69	0.69	**4.16**	**4.12**	2.81	0.70	0.73	0.67

4. Methodology validation regarding phantoms

4.1. Simulations vs. measurements with homogeneous phantoms

At this stage of the work, the dispersion law of the effective medium of a "canonical" homogeneous phantom (1.7 m tall, with a shoulder width comparable to that of the real phantom) and a "homogenized" anthropomorphic one (*Duke* from the VF suit) have been chosen to follow that of the real whole body phantom (*Kevin*, 1.7 m tall male) used for the measurements[1] [7] (Fig. 7). The aim is to be able to compare simulations and measurements with phantoms of close corpulence (trunk perimeter and shoulder width), but nothing guaranties that this dispersion law is the optimal choice for accurate statistical quantitative results (see the discussion in Section 7). The simulated realized gains of the sensor worn on phantoms' chest, *relative to the isolated one* (20), are compared in Fig. 8 for the azimuthal plane and more general "statistics" are provided in Table 3. The qualitative agreement is good and the quantitative one satisfactory enough to justify the approach. Note that the discrepancies between simulations and measurements are probably partly due to the simplified modelling of the sensor:

$$\hat{G}_{v,\text{phant}}^{\theta}(f_{\text{RAT}}, \theta, \varphi) = \bar{G}_{v,\text{phant}}^{\theta}(f_{\text{RAT}}, \theta, \varphi)/\bar{G}_{v,\text{isol}}^{\theta}(f_{\text{RAT}}, \theta, \varphi - \varphi_0)$$

$$\hat{G}_{h,\text{phant}}^{\varphi}(f_{\text{RAT}}, \theta, \varphi) = \bar{G}_{h,\text{phant}}^{\varphi}(f_{\text{RAT}}, \theta, \varphi)/\bar{G}_{h,\text{isol}}^{\varphi}(f_{\text{RAT}}, \theta, \varphi - \varphi_0) \tag{20}$$
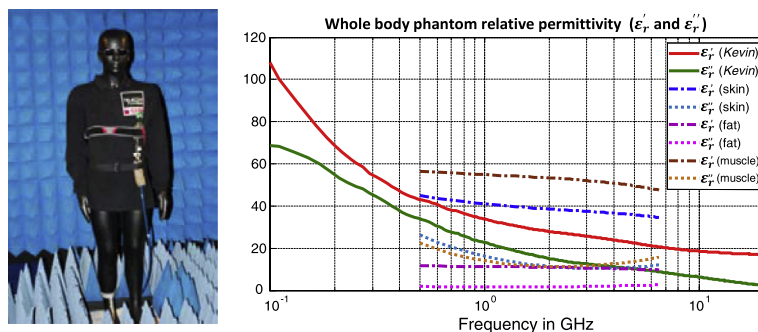

Fig. 7. (Color online.) Photograph of the sensor measurement in anechoic chamber on the whole body phantom of nickname "*Kevin*" and its dielectric characteristics.
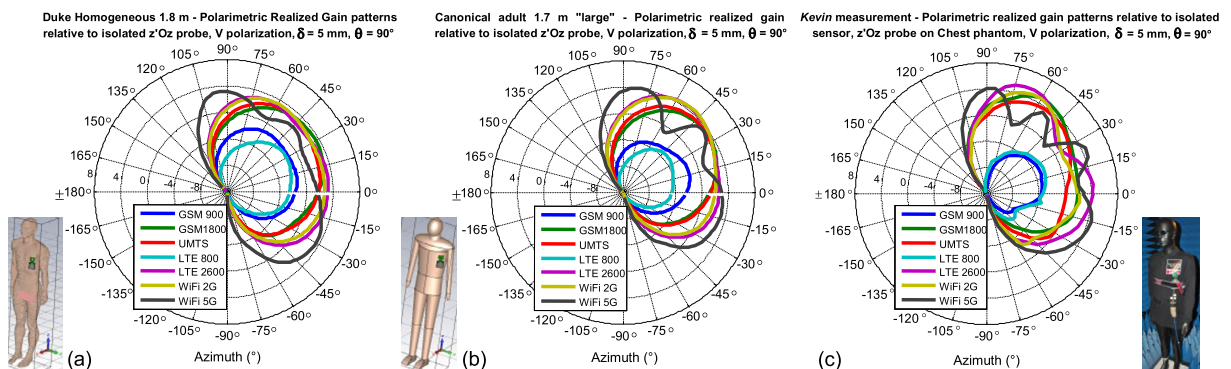

Fig. 8. (Color online.) Sensor on chest (∼ 50° from sagittal plane). Vertical probe realized gain in azimuth (dB relative to isolated), $\theta = 90°$, $\delta = 5$ mm: (a) Simulated with *Duke* anthropomorphic ("homogenised") phantom, (b) Simulated with a canonical phantom, (c) Measured on *Kevin* phantom.

4.2. Comparison of simulation results with homogeneous and inhomogeneous phantoms

The comparison of the variability of the polarimetric patterns of the worn sensor (over azimuth and elevation), here for the co-polar component of the realized gain, relative to the isolated one, between an anthropomorphic inhomogeneous phantom (*Eartha*, an 8-year-old child girl from the VF suit [12]), its "homogenized" version and a "canonical" homogeneous one is presented in Figs. 9 and 10. All phantoms are ∼ 1.3 m tall. Although non-negligible quantitative deviations can be

---

[1] Courtesy of Thierry Alves (UPEM – France) who performed these measurements with an original method that he developed.

Table 3
Relative gain variability – sensor on chest – sim. vs. measurement, $\delta = 5$ mm, $\theta \in 70°, 90°, 106°$, all φ.

| μ and σ (dB)	$\mu_{\hat{G}^{\theta}_{v.phant}}$			$\sigma_{\hat{G}^{\theta}_{v.phant}}$			$\mu_{\hat{G}^{\varphi}_{h.phant}}$			$\sigma_{\hat{G}^{\varphi}_{h.phant}}$		
	Duke	Canonic	Meas^t	Duke	Canonic	Meas^t	Duke	Canonic	Meas^t	Duke	Canonic	Meas^t
GSM 900	−10.4	−12.0	−14.6	7.9	7.9	8.4	−1.7	−1.6	1.4	3.5	3.5	4.5
GSM 1800	−9.8	−11.1	−8.7	10.8	10.8	10.5	−4.2	−4.5	−3.2	5.5	6.1	4.4
UMTS	−9.6	−10.9	−10.4	11.0	11.3	10.8	−4.4	−4.9	−3.4	5.8	6.6	4.0
LTE 800	−10.7	−12.4	−14.6	6.8	6.9	8.1	−1.2	−1.0	1.7	3.1	3.1	4.5
LTE 2600	−9.8	−10.8	−11.7	12.4	12.9	12.2	−4.7	−4.5	−3.6	7.2	7.3	5.0
Wi-Fi 2G	−9.4	−10.5	−11.1	11.6	12.4	11.0	−4.5	−4.6	−3.1	6.8	7.0	4.3
Wi-Fi 5G	−9.0	−10.2	−10.7	12.5	13.0	13.4	−6.2	−6.7	−4.6	8.9	9.5	7.5
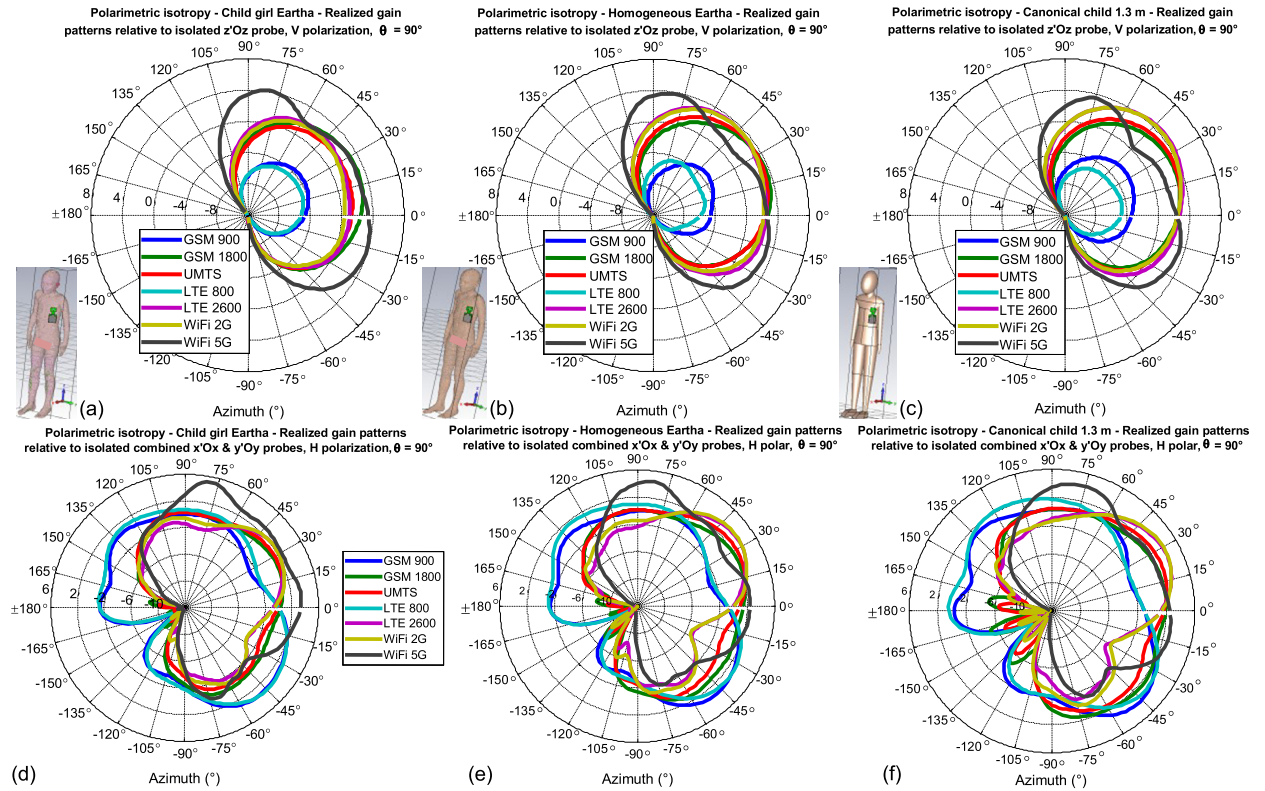
Fig. 9. (Color online.) Co-polar realized gain patterns (azimuthal plane). Sensor on *Eartha's* (a, d), *Homogenized Eartha's* (b, e) and *Canonical* (c, f) chest (∼ 50° from sagittal plane); $\delta = 5$ mm: Vertical (a–c) and combined horizontal (d–f) probes.

noted, the trends are qualitatively consistent. The former are attributed to non-negligible geometric differences and to the fact that the chosen electric properties of the effective medium of the homogeneous phantoms have not been "optimised" yet for the considered exterior EM problem (see discussion in Section 7). In addition, the sensor is very close to the body in these cases (the closest probes are 5 mm away from the body surface), whereas the low-frequency behaviour of the real sensor (typically below 1.5–2 GHz) with regard to the reflection coefficient of the probes is not well represented by the simplified model of the sensor. This may induce inaccuracies regarding near-field effects, in particular for the lower frequency bands, when the sensor is very close to the body. However, in practice, the sensor is often more away from the body. This good qualitative (and semi-quantitative) agreement can be considered as a convincing argument justifying to resort to canonical homogeneous phantoms.

5. Examples of statistical results

Examples of the statistical analysis of the field measurement errors due to the body proximity are presented for three propagation scenarios: UMa (Urban Macrocell) NLOS (No. 9) and UMa/UMi (Urban Microcell) LOS (Nos. 10 & 4). The statistics (CDF) of the field measured with a sensor worn by different phantoms on the chest, relative to the isolated measurement are presented in Fig. 11 and the first moments for the total field strength (non-polarimetric measurement) are given in Table 4. The sensor probes are placed at $\delta = 5$ mm from the body.
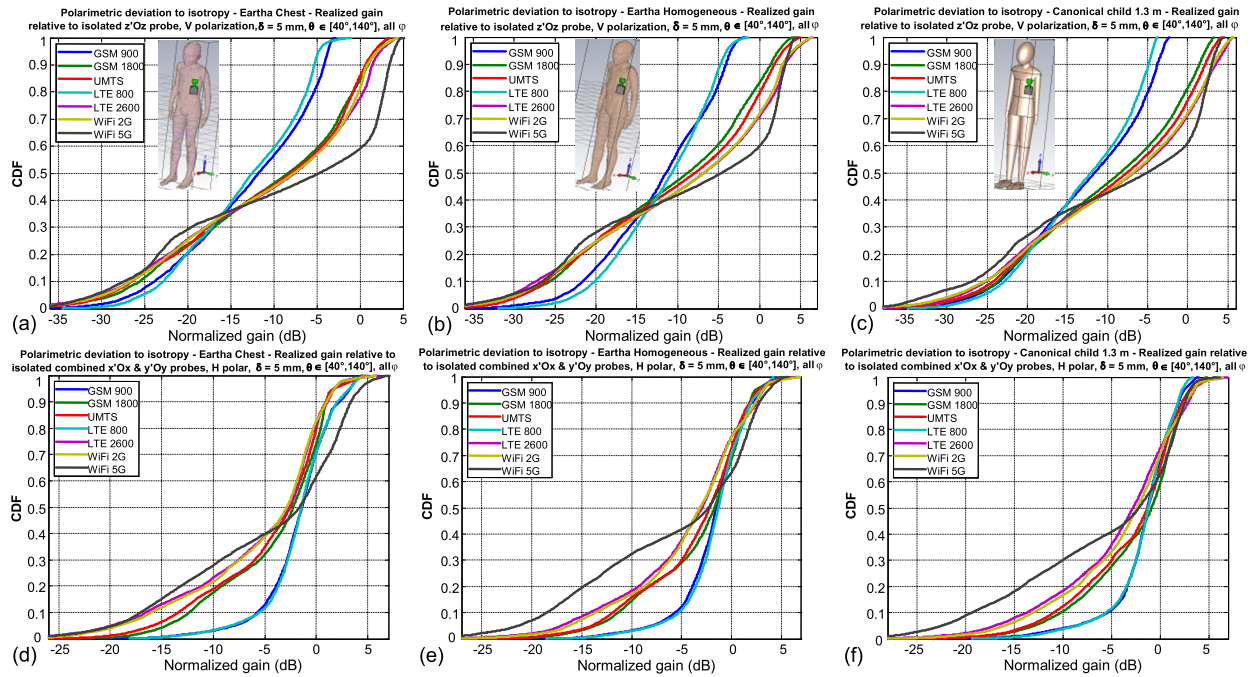
Fig. 10. (Color online.) Variability of polarimetric co-polar realized gains (dB relative to isolated). Sensor on *Eartha's* (a, d), *Homogenized Eartha's* (b, e) and *Canonical* (c, f) chest (∼ 50° from sagittal plane); δ = 5 mm, θ ∈ [40°, 140°]: Vertical (a–c) and combined horizontal (d–f) probes.
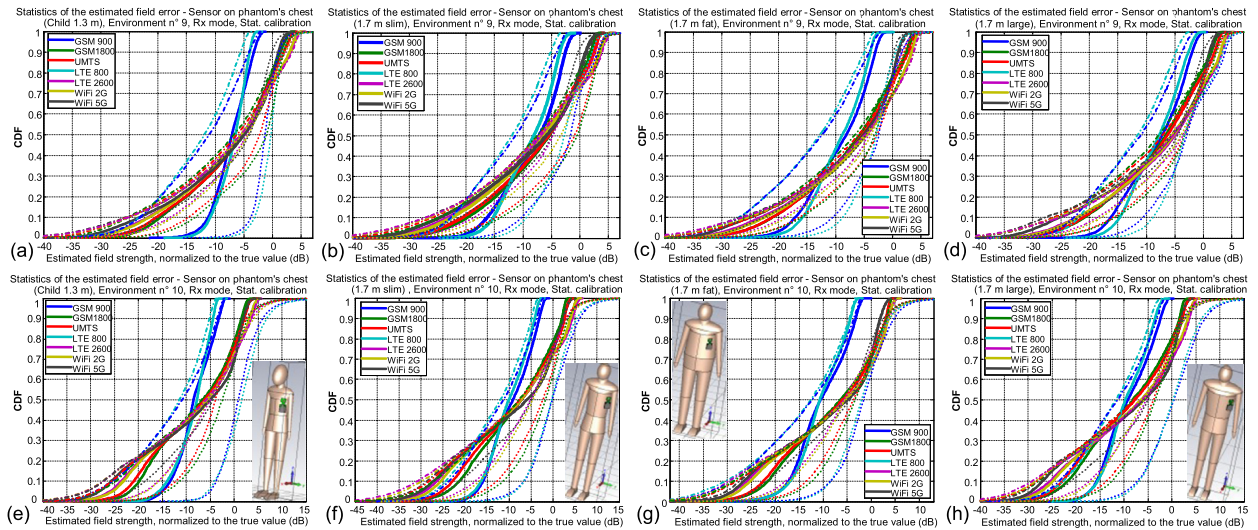

Fig. 11. (Color online.) Field strength assessment by the sensor worn on four phantom's chest (δ = 5 mm) for UMa environments, in NLOS (a–d) and LOS (e–h) conditions, relative to the *isolated* sensor; statistical normalization averaged over each environment type. Non-polarimetric (plain bold), V sensor (dashed–dotted), and H sensors (dot).

Whatever the environment (Nos. 1 to 10), the trend is an increase in the error variance with the frequency and model stature/corpulence, more pronounced in LOS conditions (which was expected, because the masking effect is not "balanced" by the large angular spread in NLOS conditions). For the lower frequency bands (LTE800/GSM900), the variance is significantly lower because the trunk perimeters (ranging typically between 60 and 90 cm) are only about 1.5 to 3λ, so that the creeping waves are less attenuated. The trends for the bias are less obvious: for the higher frequency bands, the mean error generally increases with the frequency (more clearly in LOS), whereas for the lower bands, the lesser influence of the masking effect is compensated by higher losses inside the body. In addition, the mean error typically increases with the model corpulence, but less clearly (and significantly) (Table 4).

Table 4

Mean and standard deviation of the measurement (total field) error for various models and environments.

| μ/σ (dB)	NLOS (UMa, Env. No. 9)				LOS (UMa, Env. No. 10)				LOS (UMi, Env. No. 4)			
	1.3 m slim	1.7 m slim	1.7 m large	1.7 m fat	1.3 m slim	1.7 m slim	1.7 m large	1.7 m fat	1.3 m slim	1.7 m slim	1.7 m large	1.7 m fat
GSM 900	−7.2/3.1	−8.5/5.3	−8.4/5.4	−9.3/5.5	−8.3/3.8	−9.4/5.0	−9.2/5.1	−10.4/5.5	−8.4/4.5	−9.7/5.4	−9.0/5.7	−10.4/6.0
GSM 1800	−7.3/7.9	−7.4/8.3	−8.4/8.4	−7.8/8.9	−8.1/8.3	−8.8/8.9	−9.4/9.0	−8.3/9.5	−8.2/8.6	−9.1/9.3	−9.4/9.4	−8.5/10.0
UMTS	−7.3/8.3	−7.5/8.8	−8.2/8.8	−7.5/9.0	−8.1/8.9	−9.0/9.7	−9.4/9.6	−8.4/9.8	−8.4/9.4	−9.6/10.1	−9.7/10.1	−8.8/10.4
LTE 800	−7.0/2.7	−8.8/4.6	−8.4/4.6	−9.4/4.7	−8.6/3.7	−10.1/4.6	−9.5/4.6	−10.6/4.8	−8.7/4.1	−10.4/5.6	−9.8/5.4	−10.9/5.8
LTE 2600	−7.6/9.3	−8.3/10.0	−7.5/9.7	−7.5/10.1	−8.4/10.2	−9.6/11.6	−8.9/11.0	−8.8/11.4	−8.9/10.9	−10.3/12.3	−9.5/11.7	−9.6/12.1
WiFi 2G	−7.5/9.2	−8.0/9.7	−7.6/9.5	−7.3/9.9	−8.3/10.0	−9.4/11.1	−9.0/10.7	−8.6/11.0	−8.8/10.6	−10.1/11.7	−9.5/11.3	−9.2/11.5
WiFi 5G	−8.1/9.4	−9.0/9.9	−8.8/10.0	−8.6/10.0	−8.7/10.7	−9.8/11.5	−9.6/11.3	−9.3/11.1	−9.6/11.8	−10.7/12.6	−10.1/12.3	−9.9/12.1
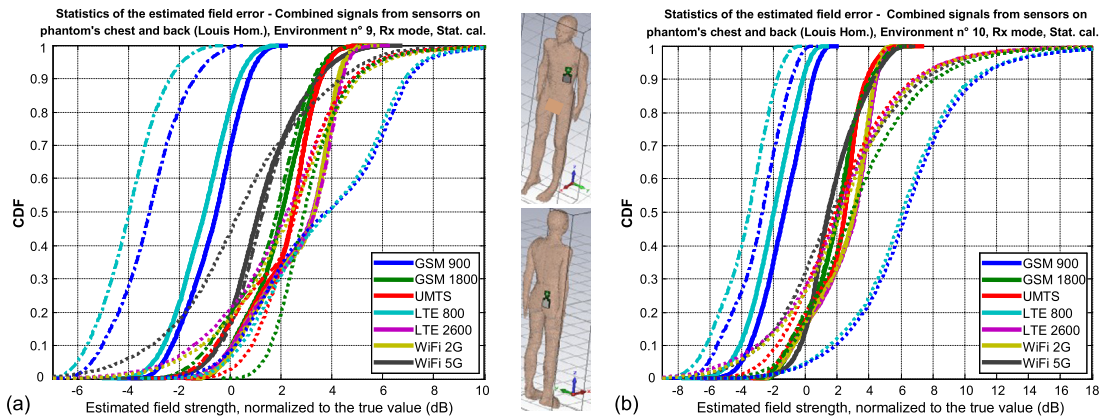
Fig. 12. (Color online.) Measurement field error after combining signals of two sensors (chest/back). for UMa environments, in NLOS (a) and LOS (b) conditions, relative to the *isolated* sensor statistical normalization averaged over all environment types. Non-polarimetric (plain), V sensor (dashed–dotted), and H sensors (dashed).

6. Possible methods of measurement errors correction

6.1. Use of several body-worn sensors

One possible method to reduce the high variance of the measurement error is to use several sensors in order to compensate for the masking effect. This simple idea is not new: it has been proposed, e.g., in [15], using three distributed sensors, but for only one band (950 MHz), simple antennas (not allowing polarimetric measurements) and without accounting for the channel properties (calibration in anechoic chamber). Besides, we have checked that placing two sensors on each side of the body brings a very significant improvement, whereas using more sensors provides only a marginal gain. Examples of results combining signals from two sensors – on the left chest and on the right back (at the rear trousers pocket level) – in NLOS and LOS conditions (environments No. 9 and 10) are shown in Fig. 12. The standard deviations of the field strength measurement (non-polarimetric) are reduced to about 1.1–1.5 dB (resp. 1.5–1.9 dB) in NLOS (resp. LOS) conditions depending on the RAT bands, to be compared, e.g., for the chest sensor alone, to about 5.2–9.3 dB (resp. 4.2–10.8 dB) in NLOS (resp. LOS) conditions. The bias (mean error) ranges between −1.1 to 2.7 dB (resp. −2.0 to 2.5 dB) in NLOS (resp. LOS) conditions; It is improved by about 5 to 7 dB (resp. 6 dB) in NLOS (resp. LOS) conditions. For the polarimetric measurements, the reduction of the variance is comparable for the vertical component (slightly lower), but less effective for the horizontal one. Note that no attempt has been made yet either to compensate for this bias with a specific calibration procedure or to search for any "optimal" combination of the sensor signals (or sensor positioning, as done in [15]). One possible way is to resort to a reference phantom, knowing however that the variability of the bias from one phantom to another is not negligible.

6.2. Possible strategy with only one body-worn sensor

Measurements with a human subject wearing two EME Spy 140® dosimeters (comprising the same triaxial sensor) on his chest, and above his head (supposed isolated and used as reference) have been performed along "routes" in various streets of Paris. Once the dosimeter is turned on, measurements automatically start. The period was set to its minimal value of 4 s. Measurements were performed "linearly" every 3 m standing still during ∼ 25 s (i.e. about seven measurements per each position along the route). In addition, among the "linear" positions, a few special measurements during which the subject was rotating on the spot every 45° (standing still during ∼ 50 s, i.e. ∼ 13 samples) were regularly performed. During the post-processing step, measurement samples of each position are averaged. A measurement example, along the "forward route" (in LOS, the BS being on subject's back) in the "rue de la Colonie" (160 m in length, i.e. ∼ 53 positions) is shown in Fig. 13. Measurements on the chest, before and after correction (based on the measurements performed during five rotations of the subject on the spot) are compared to the isolated ones in Fig. 13. The correction procedure is clearly efficient for all the bands but the Wi-Fi band, as the error is moderate and almost constant along the route because the signal comes from many sources (AP of many flats in buildings) along all the route, so that its angular spread is large.

7. Development and future works

Some simplifications – hence approximations – were intentionally done in the presented approach. In particular, the phase of the incoming (multipath) field is not taken into account, i.e. small-scale (selective) fading is not considered. It is believed that this approximation would not change the obtained results qualitatively. In addition, its quantitative effect should be moderate, because the received signals (by each probe) are averaged (in power) over each RAT band and over time/space, and that the results are obtained statistically with thousands of random samples.
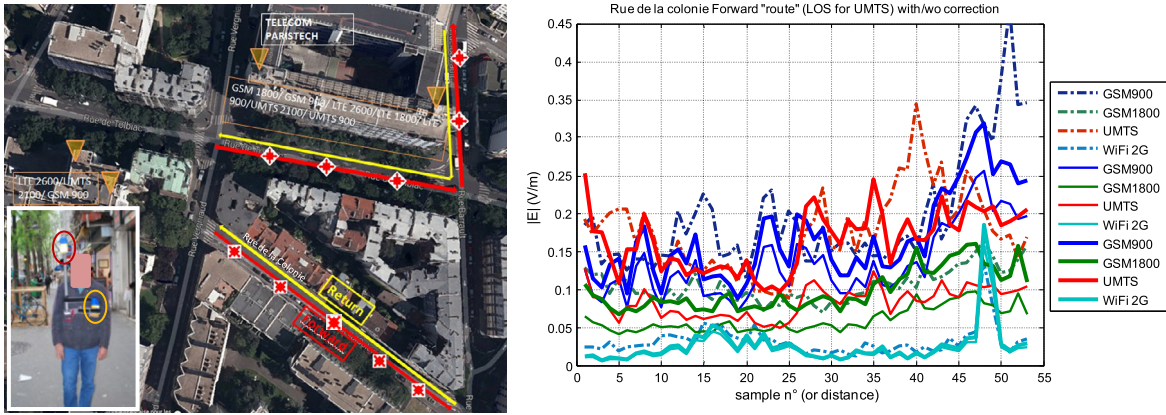
Fig. 13. (Color online.) Field measurements on a human chest, without correction (plain), with correction (plain bold), compared to the reference measurement (dashed dotted) with the dosimeter on top of the head. LOS conditions for GSM 900 and UMTS, but the BS is on the subject's back.

The electric properties of the effective permittivity (order of magnitude and dispersion law) of the used homogeneous phantoms were chosen to exactly follow the measured values of a real homogeneous whole-body phantom used for a previous measurement campaign [7,9]. This choice was done to be able to compare simulation and measurement results. Nonetheless, nothing guaranties that this is the best choice. Note, however, that the requirements for the determination of a "good" effective medium correctly modelling human tissues for *external* electromagnetic problems are completely different from those used to assess the SAR, such as "equivalent liquids" that are actually designed so as to guaranty upper bounds of the SAR measurements (i.e. safety in the worst cases).

The future developments will hence address: (i) the quantitative effect of the selective fading, accounting for the phase of the incoming waves, (ii) the design of an appropriate methodology (probably statistically based) in order to define a wide-band dispersive effective medium representing human tissues behaviour for external (but near field) EM problems, (iii) the continuation of the development of the EM simulation database, following more "educated" design of experiments, (iv) the use of more sophisticated statistical methods to assess the field measurement error induced by the body proximity, such as the computation of response surfaces, notably based on modern techniques such as polynomial chaos. Complementary analyses such as the quantitative assessment of the influence of each input parameters of the stochastic space (anthropometric parameters – stature, morphology, gender, etc. – posture, movement, sensor positioning and distance to the body, etc.) could be then rapidly derived thanks to sensitivity analyses (e.g., based on Sobol indices), (v) the development of an on-going work concerning possible strategies to estimate the environment type in which the user is performing measurements – in particular if the propagation conditions are in LOS or in NLOS – as much as possible without his help, and (vi) the study of correction schemes.

8. Conclusions

The presented results confirm that the dispersion of measurements collected by exposimeters is large. To be correct, the estimation of the variability must take into account the channel's behaviour as well as the subject's anthropometric characteristics (size, corpulence) and posture, and the sensor's positioning. In particular for the NLOS scenarios, the results obtained here confirm that the evaluation of the measurement variability due to the presence of the human body tends to be overestimated when it is only based on *intrinsic* characteristics of the worn sensor (probes and body), i.e. irrespective of the channel properties (notably its angular spread, number of MPCs, XPR_E and Rice K factor). This can be verified by comparing the variances obtained here and in [8]. Indeed, in particular in NLOS, the angular spread of the channel tends to partially compensate for the body masking effect that destroys the sensor omnidirectionality (or "isotropy"). Eventually, as it was expected, a rather clear trend can be observed in both LOS and NLOS: The variance (to a lesser extent the mean) of the error increases with the subject stature and "fatness".

Acknowledgements

Appendix A

Table 5
WINNER2/+ based environments [13,14].

Env. No.	Local environment	Visibility from BS/AP	WINNER scenario
1	Indoor small office/residential	NLOS	A1/NLOS
2	Indoor small office/residential	LOS	A1/LOS
3	Typical Urban (Hot spot)	NLOS	B1 (UMi)
4	Typical Urban (Hot spot)	LOS	B1 (UMi)
5	Metropolitan suburban	NLOS	C1 (SMa)
6	Metropolitan suburban	LOS	C1 (SMa)
7	Metropolitan O2I	NLOS	A2, B4, C4
8	Indoor (Hot spot)	LOS	B3
9	Typical UMa	NLOS	C2
10	Typical UMa	LOS	C2

References

[1] www.lexnet-project.eu.
[2] E. Conil, et al., Exposure index of EU project LEXNET: principles and simulation-based computation, in: Proc. EuCAP 2014, The Hague, The Netherlands, 6–11 April 2014.
[3] N. Varsier, et al., Deliverable D2.6: global wireless exposure metric definition, Nov. 2014, EU FP7 project Lexnet (public deliverable available on request).
[4] J. Blas, et al., Potential exposure assessment errors associated with body-worn RF dosimeters, Bioelectromagnetics 28 (7) (2007) 573–576.
[5] S. Iskra, R. McKenzie, I. Cosic, Factors influencing uncertainty in measurement of electric fields close to the body in personal RF dosimetry, Radiat. Prot. Dosim. 140 (1) (2010) 25–33.
[6] C. Roblin, Statistical analysis and error correction schemes of an UWB body-worn sensor used for electromagnetic field and exposure assessment, in: Proc. ICUWB, Paris, France, 1–3 September 2014.
[7] C. Roblin, A. Sibille, Measurement of a body-worn triaxial sensor for electromagnetic field and exposure assessment, in: Proc. EuCAP 2014, The Hague, The Netherlands, 6–11 April 2014.
[8] C. Roblin, Statistical simulations of a body-worn triaxial sensor for electromagnetic field and exposure assessment, in: Proc. URSI France Scientific Workshop, Paris, 25–26 March 2014.
[9] S. Bories, et al., Deliverable D3.2: wideband dosimeter design study & performances characterization, EU FP7, project Lexnet, Sept. 2014 (public deliverable available on request).
[10] C. Roblin, S. Bories, A. Sibille, Characterization tools of antennas in the time domain, in: Proc. IWUWBS, Oulu, June 2003.
[11] X. Begaud, et al. (Eds.), Ultra Wide Band Antennas, Wiley, 2011.
[12] http://www.itis.ethz.ch/itis-for-health/virtual-population/human-models.
[13] P. Kyösti, et al., D1.1.2 V1.2 WINNER II Channel Models, IST project WINNER II, February 2008 (public deliverable).
[14] P. Heino, et al., D5.3: WINNER+ Final Channel Models, September 2010, CELTIC project WINNER+ (public deliverable).
[15] A. Thielens, et al., Personal distributed exposimeter for radio frequency exposure assessment in real environments, Bioelectromagnetics 34 (7) (2013) 563–567.